Research Article

# Modified full-field optical coherence tomography: A novel tool for rapid histology of tissues

Manu Jain[1], Nidhi Shukla[2], Maryem Manzoor[2], Sylvie Nadolny[3], Sushmita Mukherjee[2]

[1]Department of Urology, Weill Medical College of Cornell University, New York, [2]Department of Biochemistry, Weill Medical College of Cornell University, New York, [3]LLTech SAS, Paris, France

E-mail: *Sushmita Mukherjee - smukherj@med.cornell.edu
*Corresponding author

This article may be cited as:
Jain M, Shukla N, Manzoor M, Nadolny S, Mukherjee S. Modified full-field optical coherence tomography: A novel tool for rapid histology of tissues. J Pathol Inform 2011;2:28.

Available FREE in open access from: http://www.jpathinformatics.org/text.asp?2011/2/1/28/82053

## Abstract

**Background:** Here, we report the first use of a commercial prototype of full-field optical coherence tomography called Light-CT™. Based on the principle of white light interferometry, Light-CT™ generates quick high-resolution three-dimensional tomographic images from unprocessed tissues. Its advantage over the current intra-surgical diagnostic standard, *i.e.* frozen section analysis, lies in the absence of freezing artifacts, which allows real-time diagnostic impressions, and/or for the tissues to be triaged for subsequent conventional histopathology. **Materials and Methods:** In this study, we recapitulate known normal histology in nine formalin fixed *ex vivo* rat organs (skin, heart, lung, liver, stomach, kidney, prostate, urinary bladder, and testis). Large surface and virtually sectioned stacks of images at varying depths were acquired by a pair of 10x/0.3 numerical aperture water immersion objectives, processed and visualized in real time. **Results:** Normal histology of the following organs was recapitulated by identifying various tissue microstructures. Skin: epidermis, dermal-epidermal junction and hair follicles with surrounding sebaceous glands in the dermis. Stomach: mucosa with surface pits, submucosa, *muscularis propria* and serosa. Liver: hepatocytes separated by sinusoidal spaces, central veins and portal triad. Kidney: convoluted tubules, medullary rays (straight tubules) and collecting ducts. Prostate: acini and fibro-muscular stroma. Lung: bronchi, bronchioles, alveolar ducts, alveoli and pleura. Urinary bladder: urothelium, *lamina propria*, *muscularis propria*, and *serosa*. Testis: seminiferous tubules with intra-tubular sperms. **Conclusion:** Light-CT™ is a powerful imaging tool to perform fast histology on fresh and fixed tissues, without introducing artifacts. Its compact size, ease of handling, fast image acquisition and safe incident light levels makes it well-suited for various intra-operative and intra-procedural triaging and decision making applications.

**Key words:** *Ex vivo*, histology, optical coherence tomography, organs, rat

## INTRODUCTION

In current practice for surgical interventions to treat solid tumors, intra-operative diagnosis and assessment of the surgical margins are largely provided by frozen sections.[1] In addition, other techniques such as cytology preparations (touch imprint and smear from a lesion) are also utilized where applicable.[2] The main indications for frozen sections include: (1) establishing the presence or nature of a lesion, (2) determining the adequacy of surgical resection margins, or (3) determining the adequacy of diagnosable tissue obtained.[3]

Frozen sections, despite having an overall diagnostic accuracy of 89-98% in all tissue types,[4-6]can have significant limitations, which arise mainly from tissue processing. The processing steps that are of special concern are freezing and sectioning,[2,7]which can result in freezing artifacts and physical destruction of structural integrity of the tissue, respectively. Both freezing and sectioning can thus contribute to inferior-quality slides for microscopic examination, which might in turn hinder final diagnosis. Furthermore, if such artifacts occur at the surgical margins, it may not be possible to determine whether the margin is positive or negative for malignancy,[8]which in turn has major implications regarding prognosis and follow-up treatment options. In addition, sectioning also results in significant wastage of tissue, which becomes a major concern for small biopsies that may contain the suspicious lesion in its entirety. It is also a concern in cases where it is critical to reserve tissue for ancillary definitive diagnostic studies, such as immuno-staining.[2] For this reason, most biopsy specimens are not subjected to frozen section analysis in routine clinical practice. Lastly, frozen sections result in a procedural delay of 20-30 minutes, which lengthens the time the patient stays under general anesthesia, increasing patient morbidity as well as cost of the procedure.[9]

In order to overcome these drawbacks of frozen section analysis and give a quick diagnostic impression, many high-magnification, high-resolution "optical biopsy" techniques are currently being explored to render quick intra-operative diagnostic impressions in freshly excised (unprocessed) tissue. Full-field optical coherence tomography (FFOCT) is one such promising technique.[10,11] This technology is based on the principles of white light interference microscopy. It makes use of a simple tungsten halogen lamp instead of a complex laser-based light source. The optical arrangement of FFOCT is generally based on a bulk Michelson interferometer, with identical microscope objectives in both arms. This configuration is referred to as the Linnik interferometer.[10] Due to low temporal coherence of the source, interference occurs only when the optical path lengths of the two interferometer arms are identical within ~1 $\mu$m. When a biological object is placed under the objective in the object arm, the light reflected by the reference mirror interferes with the light reflected or backscattered by the sample structures contained in a limited volume. This volume is a slice orthogonal to the objective axis, located at a depth inside the object defined by an optical path length difference of zero. The thickness of the slice is determined by the width of the fringe envelope. The extraction of the signal yields therefore an *en face* tomographic image. The signal is extracted from the large background of incoherent backscattered light using a phase-shifting method. Two interferometric images

are recorded successively with a charge-coupled device (CCD) camera, the phase being changed by 180° in the interferometer between each image. The phase shift is accomplished by a displacement of the reference mirror with a piezoelectric translation stage. The tomographic image is calculated by combining these interferometric images,[12,13] and is recorded by a detector array such as a CCD camera.

Whereas conventional optical coherence tomography (OCT) produces B-mode (axially-oriented) images like ultrasound imaging, FFOCT acquires tomographic images in the *en face* (transverse) orientation. FFOCT is thus an alternative to conventional OCT, which is able to provide ultrahigh resolution images (1-2 $\mu$m lateral resolution) that are similar to the resolution of standard histology.[10]

FFOCT is a powerful tool for performing fast histology on fresh (unprocessed, un-embedded, un-sectioned and unstained) as well as formalin-fixed *ex vivo* tissues without introducing any artifacts. It is a noninvasive technique, and does not require long sample preparation or use of contrast agents.

This study constitutes the first report on the use of a commercial prototype of FFOCT, called Light-CT™ (LLTech SAS, Paris, France). In this study, we utilize a variety of formalin-fixed *ex vivo* rat organs as model systems. The goal of this study is to assess how well the images obtained from this prototype instrument are able to recapitulate the known normal histology of these organs. In this way, we hope to provide preliminary demonstration of the clinical utility of the device in certain specific contexts, as outlined in the discussion section.

## MATERIALS AND METHODS

### Acquisition of Samples
In this study, we imaged various organs procured from freshly euthanized adult male rats, utilizing a protocol approved by the Institutional Animal Care and Use Committee. Rats are preferred models for such preliminary studies, since they are easy to procure and handle, and have a close resemblance with human anatomy and histology. We dissected various organs, including the skin, heart, lung, liver, stomach, kidney, prostate, urinary bladder and testis, immediately after carbon dioxide-induced euthanasia. Each of these organs were fixed in formalin immediately after excision (10% buffered formalin overnight at 4°C and stored thereafter in 70% ethanol at 4°C).

### Sample Preparation
The samples to be imaged were cut in cross-section (2-5 mm thick) and immersed in an isotonic solution of phosphate-buffered saline (Phosphate buffered

saline (PBS); 2.7 mM potassium chloride and 137 mM sodium chloride; pH 7.5) and placed in a sample holder (provided with the Light-CT™ system), with the surface to be imaged oriented upward. A clean silica cover-slip was placed on top of the sample. The holder cover was closed by gently moving the base of the holder so that the sample was slightly flattened, in order to provide an even imaging surface. Precaution was taken to avoid any air bubbles in the sample. A thick layer of silicone oil was applied on the glass cover-slip as the immersion medium, and the specimen was imaged through a 10x/0.3 numerical aperture (NA) water immersion objective (Olympus America, Center Valley, PA).

## Light–CT™ Instrumentation

Light-CT™ is a modified FFOCT system, which allows real-time corrections and calculations, so that visually meaningful contrast-enhanced images are displayed within seconds to minutes after the acquisition of the tomographic images. A 150-W white halogen lamp is used as a spatially incoherent light source to illuminate the whole field of the microscope objectives. The effective spectrum of the system is centered around 750 nm, with a full width at half maximum of 300 nm. At these wavelengths, the incident light level impinging on the specimen is less than 1 mW/mm$^2$.

The system consists of an upright microscope with an object and a reference arm in Linnik interferometric configuration.[10] It uses two 10x/0.3 NA water immersion objectives – one in each arm. The field of view from a single frame is ~ 1 mm × 1 mm, with 2 and 1 micron lateral and axial resolution, respectively. Large-area acquisitions can be easily obtained using an integrated image tiling option. The frame rate for the system for tomographic acquisitions is 69 Hz. Given that 60-100 images are typically averaged to obtain good-quality data, the frame rate for singleframe acquisitions is roughly 1 Hz (*i.e.* one frame/sec). This means that for a typical image shown in this paper (a single optical depth and several frames tiled) took between 2-5 min for acquisition and rendering.

## Image Acquisition

The objective lens is focused on the sample through a motorized adjustment of the whole interferometer. To secure the virtual thinness of the slice and to optimize signal to noise ratio, the instrument is always calibrated prior to scanning.

### Large-surface Acquisition

The large-field image function is used when a broad area on a sample needs to be scanned. The surface area to be imaged is defined by setting a reference point as zero and then by moving a joystick, the XY coordinates are defined and final stitched image is obtained.

### Stack Acquisition

The stack function is used to obtain depth-resolved images from the samples. The number of stacks and the distance between each stack is user-defined.

## Image Processing

The images thus acquired are processed in real time with a DICOM (Digital Imaging and Communication in Medicine) viewer and saved. They can then be read and further processed with the Image J software (National Institutes of Health, Bethesda, MD). Images acquired by this system, similar to other interference techniques, contain speckle noise.[10]We have utilized Gaussian filtering in Adobe Photoshop CS5 (San Jose, CA) to minimize speckle noise in the images presented here.

## RESULT

In this study, we imaged formalin-fixed *ex vivo* tissues from nine different rat organs, including the heart, lung, liver, skin, stomach, kidney, urinary bladder, prostate and testis. The goal was to recapitulate the normal histology of these organs, by identifying various tissue microstructures.

Figure 1 and Table 1 show images obtained from cross-sections of the skin (from flank), stomach, liver, heart, kidney and testis.

### Skin

Normal skin is composed of three tissue layers: 1) superficial epidermis, made of keratinized stratified squamous epithelium, 2) dermis, mainly comprised of collagen fibers, elastin fibers, blood vessels, nerves, lymphatics, and various skin appendages (hair follicles, sebaceous glands and sweat glands), and 3) hypodermis, a subcutaneous layer, mainly composed of adipose tissue. There is a distinct dermal-epidermal junction between the epidermis and dermis.[14]

In Figure 1a, we show that in a cross-section of rat flank skin, Light-CT™ images can be used to clearly identify the superficial epidermis (Region 1) and underlying dermis (Region 2). A dermal-epidermal junction (arrowhead) was distinctly visible. We could also recognize connective tissue in the dermis and the superficial parts of some hair follicles (arrow) and surrounding sebaceous glands (large arrowhead). At the magnification and resolution of the current clinical prototype, we were unable to differentiate the various layers of the epidermis. Hypodermis and other skin appendages were not present in our specimen [Table 1].

### Stomach

Normal stomach has four layers: 1) mucosa, the innermost layer, consisting of an epithelium lined by gastric pits, *lamina propria* composed of loose connective tissue and packed with gastric glands, and a thin layer of smooth muscle called the *muscularis mucosae*. 2) submucosa, mainly composed of fibrous connective tissue, 3) *muscularis externa (propria)*, comprised of three layers of smooth muscle bundles (inner oblique, middle

**Table 1: Tissue microstructures identified in rat ex vivo organs by Light-CT™**

| Organs imaged by Light-CT™ | Tissue microstructures identified |
|---|---|
| Skin | Stratified epidermal layer |
| | Dermis with hair follicle and surrounding sebaceous glands |
| | Dermal-epidermal junction |
| Stomach | Mucosa with surface pits |
| | Submucosa |
| | *Muscularis propria* |
| | Serosa |
| Liver | Cords of hepatocytes separated by sinusoidal spaces |
| | Central veins |
| | Portal triad (portal vein, the hepatic arteriole and the bile duct) |
| Heart | Chambers |
| | Branching striated cardiac muscle |
| Kidney | Convoluted tubules |
| | Medullary rays (straight tubules) |
| | Collecting ducts. |
| Prostate | Tubulo-alveolar gland forming acini |
| | Fibro-muscular stroma |
| | Peri-prostatic fat |
| | Capsule |
| | Blood vessels |
| Lung | Bronchi, bronchiole, alveolar duct |
| | Alveoli |
| | Pleura |
| | Blood vessels |
| Bladder | Urothelium |
| | *Lamina propria* |
| | *Muscularis propria* |
| | Serosa |
| Testis | Seminiferous tubules with germ cells |
| | Intra-luminal sperms |
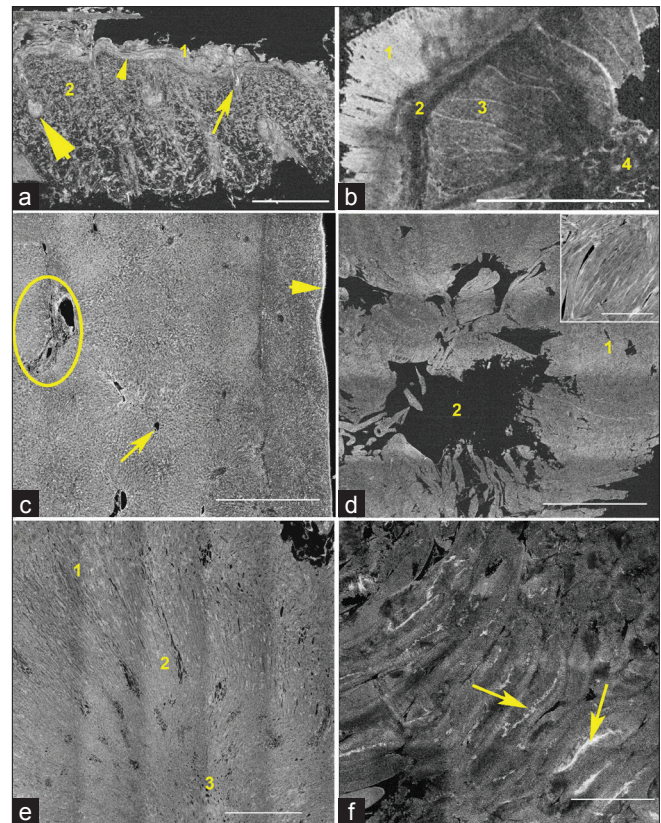


Figure 1: a: Cross-section of skin showing superficial epidermis (Region 1), dermis (Region 2), dermal-epidermal junction (arrowhead), superficial part of a hair follicle (arrow) and the surrounding sebaceous glands (large arrowhead). b: Cross-section of stomach showing mucosa with gastric pits (Region 1), submucosa (Region 2), *muscularis propria* (Region 3) and serosa (region 4). c: Cross-section of liver showing outer capsule (arrowhead), cords of hepatocytes radiating from central veins (arrow), portal triads (circle). d: Cross-section of heart showing branching muscle fibers of the myocardium (Region 1) and the ventricular chamber (Region 2). Inset shows myocardium with branching muscle bundles. e: Cross-section of kidney showing convoluted tubules (Region 1), medullary rays (Region 2) and collecting ducts (Region 3). f: Cross-section of the testis showing seminiferous tubules with intra-luminal sperms (arrows). Scale bars: 1 mm; inset in panel D = 0.5 mm

circular and outer longitudinal layers), and 4) *serosa*, the outermost connective tissue layer, which is continuous with the peritoneum.[15]

In Figure 1b, we could clearly identify these layers in a cross-sectional specimen of a rat stomach: mucosa (Region 1) with its epithelium and gastric pits, submucosa (Region 2) with fibrous connective tissue, *muscularis externa (propria)* (Region 3) comprised of smooth muscle bundles and outermost fibro-fatty layer of serosa (Region 4) [Table 1].

*Liver*
Normal liver parenchyma is mainly composed of cords of hepatocytes radiating from central veins; these cords are separated by sinusoidal spaces. Portal triad containing a branch of the hepatic arteriole, portal vein, and bile duct is seen in the liver parenchyma.[16]

In Figure 1c, we could recognize the normal architecture in a cross-sectional specimen of a rat liver, with an outer capsule (arrowhead), its cords of hepatocytes radiating from central veins (arrow pointing to a central vein), forming the main bulk of the parenchyma. Also identifiable are portal triads (marked as a circle), composed of a portal vein (biggest structure with a lumen) and two smaller luminal structures, which are the hepatic arteriole and the bile duct [Table 1].

*Heart*
Normal heart has two ventricles (right and left), separated by inter-ventricular septum and two atria (right and left). The atrium and ventricle are separated by valves (tricuspid and mitral valves). The heart wall is composed of striated, branching cardiac muscle fibers called myocardium.[14]

In Figure 1d, we could recognize branching cardiac muscle fibers of the myocardium (Region 1) and the ventricular chamber (Region 2) in a cross-sectional specimen of a rat heart. Also seen in the inset is a zoomed-in area from the heart wall showing cardiac muscle [Table 1].

### Kidney

In kidney there are two distinct components within the renal parenchyma: the cortex and the medulla. The cortex is characterized by glomeruli and highly specialized convoluted tubules. Together, the renal corpuscle and its associated tubule form a nephron. The medullary ray is the middle part of the cortical lobule or renal lobule, consisting of a group of straight tubules, running parallel to each other and finally leading into the collecting ducts. Collecting ducts are readily recognized in the renal medulla, as tubules with relatively larger lumen.[17]

In Figure 1e, we could distinguish the outer cortical area comprised of convoluted tubules (Region 1), middle area with straight tubules running parallel to form medullary rays (Region 2) and the innermost medullary area with larger-diameter collecting ducts (Region 3) in a cross-sectional specimen of a rat kidney [Table 1].

### Testis

The bulk of the volume of the normal testis is made up of seminiferous tubules that are separated by a thin layer of loose interstitium, containing Leydig cells, blood vessels, lymphatics, and connective tissue. The seminiferous tubules contain sertoli cells and spermatogonia arranged at the basement membrane and various germ cells undergoing spermatogenesis (primary and secondary spermatocytes) towards the lumen. Spermatozoon (spermatids) are seen in the lumen of the tubules.[18]

In Figure 1f, we could recognize seminiferous tubules in a cross-sectional specimen of a rat testis. These seminiferous tubule were lined by layers of germ cells and showed a distinct lumen with intra-luminal sperms (arrows) [Table 1].

### Prostate

The prostate is composed of 70% glandular elements and 30% fibro-muscular stroma. Acini are groups of secretory glands, separated by stroma. These glands are simple branching tubule-alveolar structures, lined by a double-layered epithelium consisting of the inner secretory and outer basal layers. The prostate gland is enveloped by a fibrous capsule and peri-prostatic fat.[19]

In Figure 2, we were able to identify prostatic acini (Region 1) and fibro muscular stroma (Region 2) in a cross-sectional specimen of a rat prostate. We could also identify the papillary folds of the acinar glands, as shown in Inset a (zoomed in relative to the main image). In addition, the capsule (shown by arrow), peri-prostatic fat (Region 3) and some large blood vessels (Region 4) were also recognized [Table 1].

### Lung

The normal lung tissue is mainly composed of thin-walled alveoli, giving it a fine lace-like appearance. The branching respiratory airway of the lung starts with the
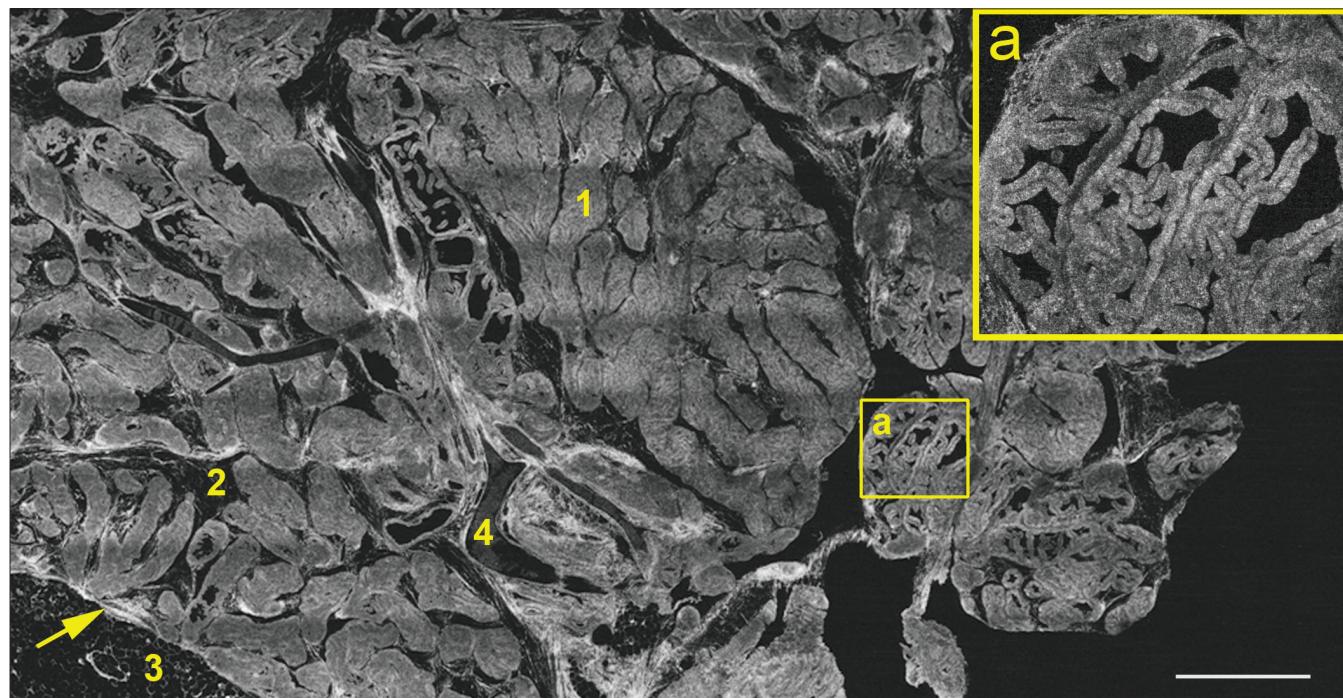


**Figure 2: Cross-section of prostate gland showing prostatic acini (Region 1) and fibromuscular stroma (Region 2), capsule (arrow), peri-prostatic fat (Region 3) and blood vessels (Region 4). Papillary folds of the acinar glands are shown in Inset a (zoomed in relative to the main image). Scale bar: 1.5 mm**

bronchus at the hilum and gives rise to smaller-caliber airways, called bronchioles. These bronchioles then proceed into the alveolar duct, which eventually ends into a blind sac, called the alveolar sac, where major exchange of gases takes place. This branching respiratory airway is accompanied all the way by pulmonary and bronchial arteries. The lung is surrounded by pleura, a thin layer of connective tissue which is lined by mesothelial cells.[20]

Figure 3 shows the normal architecture in a cross-section of the rat lung. The branching respiratory airway was readily recognized, starting, as shown in Inset a, with the bronchus (Region 1) and its accompanying pulmonary vessel (Region 2) at the hilum. As shown in Inset b, we were also able to identify a bronchiole (Region 1), leading into an alveolar duct Region 2).The majority of the lung parenchyma, as seen in Inset c, is composed of alveoli (Region 1) and surrounded by visceral pleura (Region 2) [Table 1].

### Urinary Bladder

The urinary bladder is composed of four layers: (a) urothelium, (b) *lamina propria*, (c) *muscularis propria*, and (d) *adventitia* or *serosa*. Normal urothelium is a stratified transitional epithelium, which is three to seven cell layers thick. The underlying *lamina propria* is made of collagen bundles and medium-sized blood vessels. The *muscularis propria* has three layers (inner and outer longitudinal and middle circular layer). *Serosa* the outermost layer, is mainly composed of connective tissue.[21]

In Figure 4, we show that we could identify all the layers in a cross-section of the rat urinary bladder. Inset a shows stratified urothelium (Region 1) and underlying connective tissue of *lamina propria* (Region 2). Inset b shows smooth muscular bundles of *muscularis propria* (Region 3) and the outermost layer of *serosa* (Region 4) [Table 1].

### DISCUSSION

With the images obtained from formalin-fixed (unstained and unprocessed) rat organs (heart, lung, liver, skin, stomach, kidney, urinary bladder, prostate and testis) using Light-CT™, we could successfully recapitulate the normal histology of these organs, by identifying various tissue microstructures. In skin, we could identify the epidermis, dermal-epidermal junction and dermis with the skin appendages (hair follicles and surrounding sebaceous glands, in our case). We could also clearly identify layers of the stomach wall, *i.e.* the mucosa with surface pits, submucosa, *muscularis propria/externa* and serosa. Likewise, normal liver architecture was recognized as having radiating cords of hepatocytes from central veins, separated by sinusoidal spaces. Portal triad composed of a portal vein, the hepatic arteriole and the bile duct, was also seen clearly. Heart was recognized by
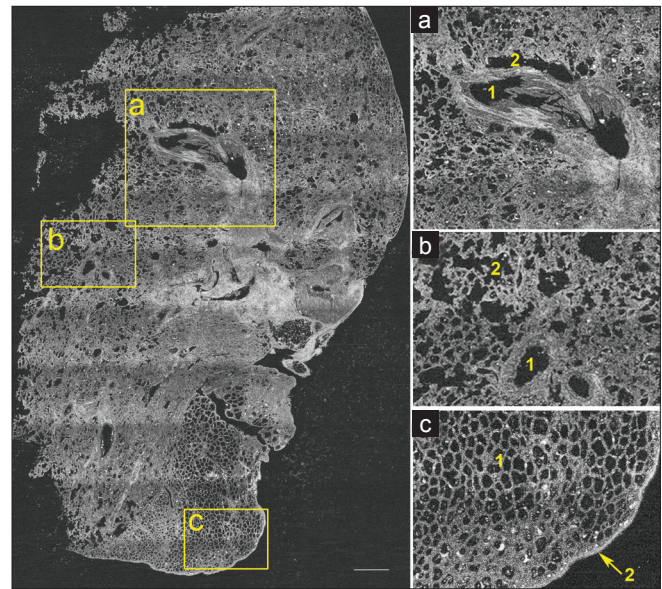


**Figure 3: Cross-section of lung. Inset a showing bronchus at the hilum (Region 1) and its accompanying pulmonary vessel (Region 2). Inset b shows a bronchiole (Region 1) and an alveolar duct (Region 2).The majority of the lung parenchyma, as seen in Inset c, is composed of alveoli (Region 1) and surrounded by visceral pleura (Region 2). Scale bar: 0.5 mm**
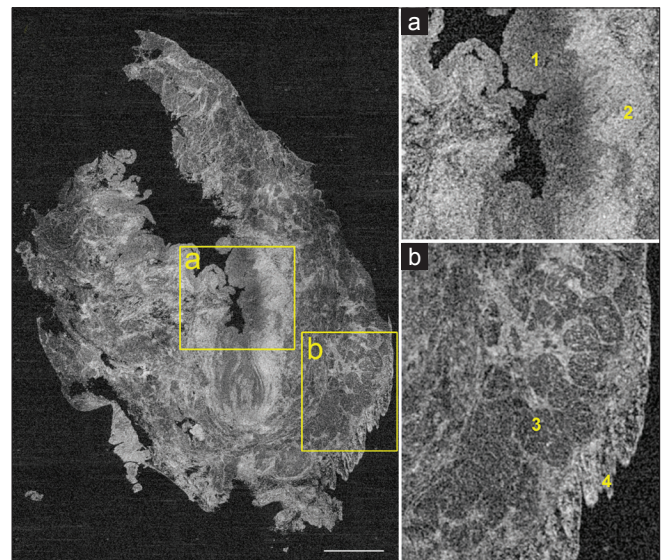


**Figure 4: Cross-section of urinary bladder. Inset a shows stratified urothelium (Region 1) and underlying connective tissue of lamina propria (Region 2). Inset b shows smooth muscular bundles of *muscularis propria* (Region 3) and the outermost layer of serosa (Region 4). Scale bar: 0.5 mm**

its branching cardiac muscles and chambers. In kidney, we were able to identify convoluted tubules, medullary rays (straight tubules) and collecting ducts in the medulla. Normal prostate architecture was seen as having tubulo-alveolar glands forming acini, embedded in fibro-muscular stroma. Prostatic capsule and peri-prostatic fat was also identifiable. The lace-like pattern formed by alveoli of the lung was evident, and so was the branching

respiratory airway (bronchi, bronchiole and alveolar duct). Lung was seen enveloped by pleura. All four layers of the urinary bladder *i.e.* the urothelium, *lamina propria*, *muscularis propria*, and *adventitia* or *serosa*, were clearly seen. Testis showed seminiferous tubules lined by layers of germ cells and intra-luminal spermatozoon.

As discussed above some advantages of Light-CT™ are the speed and simplicity with which tomographic images of relatively large areas of tissue can be obtained. The vertical depth to which usable images can be obtained depends on the optical properties of the tissue, and as shown here, is quite variable. Furthermore, the use of a halogen lamp as the light source ensures that the technique is relatively safe for use in human tissue. In fact, the incident power under the objective is ~1 mW/mm$^2$, which is significantly lower than the safety limits for near-infrared wavelengths recommended both by the European and the American standards. Confocal microscopy,[22] a competitive approach, can provide similar resolution images as FFOCT in a clinical setting. However, these devices have several drawbacks, including (1) use of relatively high-powered lasers as their light source, (2) utilization of high NA objectives thus resulting in smaller fields of view, (3) use of visible light for illumination, thereby limiting the depth of imaging in tissue, and (4) longer time to generate images of comparable dimensions, since the images here are generated by raster scanning a focused laser beam.

The major limitation of the current clinical prototype of FFOCT is the absence of cellular and nuclear details in most tissues, as shown in our results. This is predominantly a function of the use of a relative low NA (0.3) objective in this prototype, along with the presence of speckle artifacts that further reduces effective resolution. Consequently, it is our opinion that while the current prototype is excellent for a quick diagnostic impression on clinical specimens where a decision can be made on architectural information alone, it will require better lateral resolution for successfully addressing clinical questions that require cellular and/or nuclear information.

Some examples of clinical contexts where relatively low-resolution architectural information will suffice to determine if the biopsy tissue is representative of disease include: (1) increased fibrosis indicating cirrhotic liver disease or interstitial lung disease, and (2) assessment of margins in surgical management of solid tumors, where clusters of malignant cell at the margin would indicate a positive margin. However, given the current resolution, the latter application would work only in certain organs, where the architecture of the normal tissue is quite different from the morphology of the malignant cells. One such example would be breast cancer lumpectomy procedures, where clusters of malignant cells can be easily identified in an otherwise adipocyte-rich milieu.[23]

Moreover, the breast is not a good model for frozen section analysis due to the presence of adipose tissue (which does not freeze well).[24] Thus, a technique such as Light-CT™ may provide a viable alternative for intra-surgical guidance in such contexts, thereby potentially improving surgical outcomes. This will not be the case, however, if the organ itself is cellular, since the resolution of this device is inadequate in the current clinical prototype to distinguish normal cells from malignant ones.

Light-CT™, in its current form, also opens up the possibility for certain novel clinical applications. One of the most immediate and reliable applications could be in the assessment of the adequacy of diagnostic material obtained on biopsy. For example, cancers in various lumenal organs (*e.g.*, the esophagus, the colon, the bladder) originate from the innermost layers of epithelial cells, and the stage of the cancer is diagnosed based on how deep the cancer has invaded into the underlying tissue layers.[25] Taking bladder cancer as an example, the treatment options for non-muscle invasive vs. muscle invasive cancers are quite different.[26] However, current cystoscope guided biopsies are often not deep enough – thus not allowing the pathologist the make a definitive diagnosis regarding the invasiveness of the tumor. This might necessitate the patient to undergo a repeat biopsy procedure, increasing both the psychological trauma and the cost.

Current methods used in pathology to offer immediate impressions and evaluate specimen adequacy, such as frozen section analysis and Diff-Quick® examination of fine needle aspirations, may introduce irreversible freezing and air drying artifacts, respectively, thereby making a definitive final diagnosis on that specimen nearly impossible in certain cases. For this reason, biopsy specimens are not routinely subjected to frozen section analysis, since these small specimens may contain the suspicious lesion in its entirety. Light-CT™, on the other hand, does not require any tissue preparation, and introduces no freezing artifacts or tissue destruction and thus, may become a "triage" technique for biopsies. All biopsies removed for later diagnostic pathology can be quickly assessed with Light-CT™, thereby ensuring that the biopsies being sent for diagnostic pathology by formalin-fixed, paraffin-embedded (FFPE) histopathology are adequate.

In the future, many of the limitations outlined for the current clinical prototype can be overcome. For example, laboratory based systems have already been described with much higher resolution (0.7 × 0.9$\mu$m axial and lateral resolution, respectively, using a pair of 40x/0.8 NA objectives).[27] Such systems should be able to provide the necessary resolution, for example, to identify cellular and nuclear features that will allow the distinction between normal and malignant cells.

Similarly, laboratory based systems using a Xenon flash lamp as the light source have been described,[27] where the frame rates can be increased to 10 microsecond/frame where the frame rates can be *in vivo* systems, where objects are not as stationary. In this system, rather than producing two phase-opposed images by path length modulation and capturing them consecutively on a single CCD camera (like in Light-CT™), a quarter-wave plate introduced in one of the interferometric arms is used to create a λ/2 phase retardation between the object and the reference. A polarizing beam-splitter then splits the interference signal into two phase-opposed interference images, which are simultaneously captured by two identical CCD cameras. The final tomographic image is then calculated from this pair of interference images.

Using such improved instrumentation, FFOCT has been used with rat, mouse and porcine ocular tissue to generate images of the retina at cellular resolution,[29,30] as well as to create three-dimensional images of the mouse embryo in a study of the establishment of the anterior-posterior axis in embryogenesis.[31]

In addition, several experimental approaches are being considered to improve the depths in tissue to which usable images can be obtained using FFOCT. For example, a careful analysis of the image quality with increasing depth has indicated that the deterioration of image quality with depth is not primarily due to a damping of ballistic photons, but rather due to a wavefront distortion generated by tissue.[28] Thus, adaptive optics can be considered in future designs to correct for such mismatch, thereby increasing the effective depth of imaging.

In addition, several approaches are being considered for *ex vivo* specimens to increase contrast by using chemical agents that alter the optical properties of the tissue (*e.g.*, acetic acid, aluminum chloride).[32,33] Future studies will address the efficacy of such methods and how tissues thus treated behave in terms of subsequent gold standard histopathology.

In conclusion, this study presents evidence, using a commercial prototype for clinical FFOCT, that such devices can serve as powerful imaging tools to perform several clinically meaningful quick assessments of freshly excised tissue, in order to provide yes/no answers to guide surgeons and other physicians in procedures such as assessment of fibrosis, evaluation of surgical margins, and confirming the adequacy of biopsied tissue for subsequent definitive histopathological diagnoses. The procedure is fast, easy to learn, simple to use, and safe both in terms of the light exposure and in terms of maintaining the excised tissue in an unprocessed state, so that they can later be processed for standard histopathology.

## REFERENCES

1. Lessells A, Simpson J. A retrospective analysis of the accuracy of immediate frozen section diagnosis in surgical pathology. Br J Surg 1976;63:327-9.
2. Taxy J. Frozen section and the surgical pathologist: A point of view. Arch Pathol Lab Med 2009;133:1135-8.
3. Sienko A, Allen TC, Zander DS, Cagle PT. Frozen section of lung specimens. Arch Pathol Lab Med 2005;129:1602-9.
4. Nakazawa H, Rosen P, Lane N, Lattes R. Frozen section experience in 3000 cases: Accuracy, limitations, and value in residence training. Am J Clin Pathol 1968;49:41-51.
5. Ishak K. Benign tumors and pseudotumors of the liver. Appl Pathol 1988;6:82-104.
6. Nagasue N, Akamizu H, Yukaya H, Yuuki I. Hepatocellular pseudotumor in the cirrhotic liver. Report of three cases. Cancer 1984;54:2487-94.
7. Weinberg E, Cox C, Dupont E, White L, Ebert M, Greenberg H, *et al*. Local recurrence in lumpectomy patients after imprint cytology margin evaluation. Am J Surg 2004;188:349-54.
8. Lechago J. Frozen section examination of liver, gallbladder, and pancreas. Arch Pathol Lab Med 2005;129:1610-8.
9. McLaughlin SA, Ochoa-Frongia LM, Patil SM, Cody HS 3rd, Sclafani LM. Influence of frozen-section analysis of sentinel lymph node and lumpectomy margin status on reoperation rates in patients undergoing breast-conservation therapy. J Am Coll Surg 2008;206:76-82.
10. Dubois A, Boccara C. Full-field OCT. Med Sci (Paris) 2006;22:859-64.
11. Dubois A, Grieve K, Moneron G, Lecaque R, Vabre L, Boccara C. Ultrahigh-resolution full-field optical coherence tomography. Appl Opt 2004;43:2874-83.
12. Dubois A, Vabre L, Boccara AC, Beaurepaire E. High-resolution full-field optical coherence tomography with a Linnik microscope. Appl Opt 2002;41:805-12.
13. Vabre L, Dubois A, Boccara C. Thermal-light full-field optical coherence tomography. Opt Lett 2002;27:530-2.
14. Wilson F. Histology Image Review. New york: Mcgraw-Hill; 1999.
15. Semrin M. Feldman: Sleisenger and Fordtran's Gastrointestinal and Liver Disease. 9th ed, Vol. 1. Philadelphia: W.B. Saunders; 2010.
16. Misdraji J. Embryology, Anatomy, Histology, and Developmental Anomalies of the Liver., in *Feldman: Sleisenger and Fordtran's Gastrointestinal and Liver Disease*. Philadelphia: Saunders; 2010.p. 1203-4.
17. Anderson J. Surgical Anatomy of the Retroperitoneum, Adrenals, Kidneys, and Ureters, in Wein: Campbell-Walsh Urology. In: Wein AJ, editor. Philadelphia: Saunders Elsevier: PA; 2007.
18. Sigman M. Reproductive and Sexual Function., in *Wein: Campbell-Walsh Urology*. In: WEIN AJ, editor. Philadelphia: Saunders Elsevier: PA; 2007.
19. James D. Anatomy of the Lower Urinary Tract and Male Genitalia., in *Wein: Campbell-Walsh Urology*. In: Wein AJ, editor. Philadelphia: Saunders Elsevier: PA; 2007.
20. Husain A. The Lung, in *Robbins and Cotran Pathologic Basis of Disease*. In: Kumar V, editor. Philadelphia: Saunders; 2009.
21. Epstein J, Amin M, Reuter V. Biopsy interpretation of the bladder. 2nd ed. Philadelphia, PA: Lippincott Williams and Wilkins; 2010.
22. Kempe M, Rudolph W, Welsch E. Comparative study of confocal and heterodyne microscopy for imaging through scatteringmedia. J Opt Soc Am 1996;A13:46-52.
23. Schedin P, Hovey RC. Editorial: The mammary stroma in normal development and function. J Mammary Gland Biol Neoplasia 2010;15:275-7.
24. Nguyen FT, Zysk AM, Chaney EJ, Kotynek JG, Oliphant UJ, Bellafiore FJ, *et al*. Intraoperative evaluation of breast tumor margins with optical coherence tomography. Cancer Res 2009;69:8790-6.
25. Kirkali Z, Chan T, Manoharan M, Algaba F, Busch C, Cheng L, *et al*. Bladder cancer: Epidemiology, staging and grading, and diagnosis. Urology 2005;66:4-34.
26. Patel A, Campbell S. Current trends in the management of bladder cancer. J Wound Ostomy Continence Nurs 2009;36:413-21.
27. Grieve K, Moneron G, Guiot E, Boccaara, AC. Full-field OCT: *ex vivo* and in vivo biological imaging applications. Proc. of SPIE 2005;5690:31-38.
28. Boccara C, Gigan S, Roth M, Binding J, "Optical coherence microscopy (OCM) and full field OCT (FFOCT) for wavefront correction in dense tissues," in biomedical optics, OSA technical digest (CD) (Optical Society of America, 2010), paper BTuD14.
29. Grieve K, Paques M, Dubois A, Sahel J, Boccara C, Le Gargasson JF, *et al*.

Ocular tissue imaging using ultrahigh-resolution, full-field optical coherence tomography. Invest Ophthalmol Vis Sci 2004;45:4126-31.

30. Dubois A, Moneron G, Grieve K, Boccara AC. Three-dimensional cellular-level imaging using full-field optical coherence tomography. Phys Med Biol 2004;49:1227-34.

31. Perea-Gomez A, Camus A, Moreau A, Grieve K, Moneron G, Dubois A, *et al.* Initiation of gastrulation in the mouse embryo is preceded by an apparent shift in the orientation of the anterior-posterior axis. Curr Biol 2004;14:197-207.

32. Scope A, Mahmood U, Gareau DS, Kenkre M, Lieb JA, Nehal KS, *et al*. In vivo reflectance confocal microscopy of shave biopsy wounds: Feasibility of intraoperative mapping of cancer margins. Br J Dermatol 2010;163:1218-28.

33. Rajadhyaksha M, Menaker G, Flotte T, Dwyer PJ, González S. Confocal examination of nonmelanoma cancers in thick skin excisions to potentially guide mohs micrographic surgery without frozen histopathology. J Invest Dermatol 2001;117:1137-43.